PCCP

ROYAL SOCIETY OF CHEMISTRY

PAPER

View Article Online
View Journal | View Issue

Electronic and optical properties of TiO_2 nanotubes and arrays: a first-principles study†

Cite this: *Phys. Chem. Chem. Phys.*, 2014, **16**, 11519

Qiangqiang Meng,[a] Zhaoyong Guan,[a] Jing Huang,[ab] Qunxiang Li*[ac] and Jinlong Yang[ac]

Received 13th March 2014, Accepted 22nd April 2014

DOI: 10.1039/c4cp01077a

www.rsc.org/pccp

Recently, the synthesis, properties, modifications, and applications of TiO_2 nanomaterials have attracted much research attention. Here, based on extensive density functional theory calculations, we explored the stability, electronic structures and optical absorption properties of single-walled TiO_2 nanotubes (SWTONTs) and TiO_2 nanotube arrays (TONTAs), which are constructed from anatase TiO_2(101) monolayers and bilayers, respectively. We obtained the stable D_{nd} (n = 3–5) and $S_{2n}(-n, n)$ (n = 3–9) SWTONTs, and found that SWTONTs energetically prefer S_{2n} symmetry. Compared with $S_{2n}(-n, n)$ SWTONTs, the calculated Young's moduli of $D_{nd}(-n, n)$ SWTONTs are more stiff due to their relatively large strain energies. The band gaps of hexagonal TONTAs are not sensitive to their apertures, which are less than that of TiO_2 bilayers. The narrow band gaps of TONTAs originate from the edge states mainly contributed by the Ti and O atoms at the core region. The calculated optical absorptions of both SWTONTs and TONTAs display anisotropic features. These results clearly reveal that the electronic and optical properties of TiO_2 nanostructures are strongly associated with their symmetry, dimensions and morphology, which provide useful insights into the understanding of the related experimental observations.

Introduction

The first highly ordered arrays of TiO_2 nanotubes were reported by Zwilling and co-workers through a simple optimized electrochemical anodization of a titanium metal sheet in 1999.[1,2] Since then, intense research activities on synthesis, properties, modifications, and applications of various TiO_2 nanomaterials have been conducted.[3] Nowadays, various methods,[4] including the use of nanoporous alumina as the template,[5] hydro/solvothermal techniques,[6] and the anodization of titanium in an electrolyte,[7] have been adopted to synthesize TiO_2 nanotubes and arrays. The shape or morphology of TiO_2 tubes can be effectively controlled in experiments to produce the freestanding,[8] nanopores with hexagonal structures,[9,10] and hexagonal compact packed TiO_2 nanotube arrays (TONTAs).[11–13] These anatase TONTAs prefer the (004) orientation along the tube axis.[11] Due to the large internal surface area and the highly order geometrical structures, TONTAs possess outstanding charge transport and carrier lifetime properties since they have electron percolation pathways for vectorial charge transfer between interfaces.[14] These excellent properties make them suitable for various applications, *i.e.* sensors,[15] dye sensitized solar cells,[16,17] hydrogen generation from water photo electrolysis,[18] and photo reduction of CO_2 under outdoor sunlight.[19]

In the past few years, atomic structures, geometric parameters and morphologies have always been used to understand the photocatalytic activity of TiO_2 nanotubes and arrays.[3,20,21] Compared with extensive experimental investigations, only a few theoretical studies have been carried out to examine the structures and properties of TiO_2 nanotubes at the atomic scale.[22–35] Several different crystal surfaces, such as the anatase (101)[22–25] and (001)[26] surfaces, and rutile (110)[27,28] and (001)[29] surfaces, of TiO_2 thin sheets have been rolled into TiO_2 nanotubes. Moreover, TiO_2 nanotubes have also been constructed by using dititanate,[36] trititanate[37] and lepidocrocite[38] sheets, Hex-ABC structures,[39] and fluorite type TiO_2(111) thin films.[40] These research activities focused on the atomic structures, orientations, band gap modifications and photocatalytic efficiency. The recent progress can be seen from the review paper by Hossain *et al.* on structural, electronic and optical properties of TiO_2 nanotubes.[41]

Previously, much attention has been paid to single-walled TiO_2 nanotubes (SWTONTs).[42–44] However, the relationship between the atomic structures and electronic properties of SWTONTs has been rarely studied so far.[28,45] To our knowledge, no comprehensive

---

[a] *Hefei National Laboratory for Physical Sciences at the Microscale, University of Science and Technology of China, Hefei, Anhui 230026, China. E-mail: liqun@ustc.edu.cn*

[b] *School of Materials and Chemical Engineering, Anhui University of Architecture, Hefei, Anhui 230022, China*

[c] *Synergetic Innovation Center of Quantum Information and Quantum Physics, University of Science and Technology of China, Hefei, Anhui 230026, China*

† Electronic supplementary information (ESI) available: Test calculated results including band gaps and band structures by using the HSE06/PBE functionals and the DFT + U method, and optimized structures of D_{4d} and $S_8(-4, 4)$ SWTONTs. See DOI: 10.1039/c4cp01077a

ab initio calculations have been carried out to investigate TONTAs with different apertures till now. In this work, we performed extensive density functional theory (DFT) calculations to examine SWTONTs and TONTAs, which are constructed from anatase $TiO_2(101)$ monolayers and bilayers, respectively. Our attention focused on their stability, geometric symmetry, electronic properties and optical absorption. Theoretical results clearly reveal that the stability and electronic structures of SWTONTs are strongly related to the initial geometric symmetry. We obtained three stable SWTONTs with D_{nd} (n = 3–5) symmetry with stiff elastic properties, and all SWTONTs (n = 3–9) prefer the structure with S_{2n} symmetry. The band gaps of the TONTAs are relatively small than that of TiO_2 bilayers, which results in the red optical absorption onset. These theoretical predictions indicate that the electronic and optical properties of TiO_2 nanostructures can be effectively controlled by changing their symmetry, dimensions, and structures, which provide useful insights into the understanding of the related experimental observations.

Computational details

We performed DFT calculations by using the Vienna ab-initio simulation package (VASP).[46,47] The interaction between the core and valence electrons was described using the frozen-core projector augmented wave approach.[47] The exchange–correlation interaction was described by using Perdew–Burke–Ernzerhof generalized gradient approximation (PBE-GGA).[48] A plane-wave cutoff energy of 520 eV was consistently used. The lattice constants and all atomic positions were fully relaxed by the conjugate gradient procedure until the atomic forces were smaller than 0.02 eV $Å^{-1}$, and the tolerance for energy convergence was set to 10^{-5} eV.

A Monkhost–Pack mesh of $4 \times 10 \times 1$ k-points was used to sample the Brillouin zone of TiO_2 sheets, while a $1 \times 1 \times 6$ k-points mesh was used for SWTONTs and TONTAs. We performed test calculations using the Heyd–Scuseria–Ernzerhof (HSE06) hybrid functional[49,50] and DFT + U.[51,52] Compared with the results of the PBE-GGA method, the features of the band structure are not obviously changed, but the band gap of TiO_2 bulk was predicted to be 3.26 eV using the HSE06 hybrid functional, which agrees well with the experimental value.[53] However, the computational cost using the HSE06 hybrid functional was expensive. The HSE06 calculations for the large TiO_2 nanotubes and arrays were not bearable for our current resources. The test DFT + U calculated results show that this method cannot precisely produce the band structures of TiO_2 sheets (see Fig. S1 in the ESI†). Therefore, instead of HSE06 and DFT + U, the PBE-GGA method was adopted in our calculations. The optimized lattice constants (a = 3.82, c = 9.69 Å) of TiO_2 bulk agree well with the experimental results (a = 3.78, c = 9.51 Å).[54] The PBE-GGA functional underestimates the band gaps of metal oxides, *i.e.* the band gap of TiO_2 bulk is about 1.92 eV, needing a shear factor (about 1.37 eV, see Table S1 in the ESI†) compared with the HSE06 results. Moreover, the PBE-GGA is an often adopted method to describe the geometric and electronic structures of transition metal oxides.[55–57]

Results and discussion

A. Single-walled TiO_2 nanotubes

Firstly, we cut a monolayer from the (101) surface of anatase TiO_2 bulk, as shown in Fig. 1(a). When this rectangular monolayer was rolled up along the a direction, a $(-n, n)$ SWTONT was obtained. To obtain a (n, n) SWTONT, the direction of rolling up should be along the b axis. In this work, we focused on SWTONTs with $(-n, n)$ chirality since they are more stable than those with (n, n) chirality.[23] In our calculations, the lattice constant (c) along the tube axis (Z direction) and all atomic positions were fully optimized. The optimized structural parameters are summarized in Table 1. Here, we omitted the translation symmetry and used point groups to label the symmetry of these rolled up SWTONTs for clarity. Here, we obtained the stable D_{nd} (n = 3–5) and S_{2n} (n = 3–9) SWTONTs. Note that if $n \geq 6$, the $D_{nd}(-n, n)$ SWTONTs are unstable and will change into S_{2n} symmetry automatically. As examples, the optimized D_{4d} and $S_8(-4, 4)$ SWTONTs are shown in Fig. 1(b) and (c), respectively, which have polygon- and circle-like structures (see Fig. S2 in ESI†). Due to the curvature effect, the Ti–O bond lengths in the outer and inner layers are somewhat different from the Ti–O distances (1.81 and 1.91 Å) in the TiO_2 monolayer. For example, the Ti–O bond lengths are about 1.86 and 1.84 Å in the outer and inner layers in the $D_{4d}(-4, 4)$ SWTONTs, and the corresponding values vary

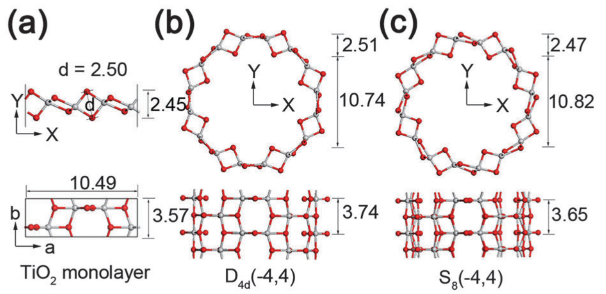

Fig. 1 (a) The side and top views of the TiO_2 monolayer. (b) The side and top views of the $D_{4d}(-4, 4)$ SWTONT, (c) the $S_8(-4, 4)$ SWTONT. Here, the grey and red balls stand for Ti and O atoms, respectively.

Table 1 The diameter (D in Å), wall thickness (T in Å), the lattice constant along the tube axis (c in Å), the energy gap (E_g in eV) and the strain energy (E_S in eV) of D_{nd} and S_{2n} SWTONTs

Parameter	D	T[a]	c	E_g	E_S
$D(-3, 3)$	12.29	2.51	3.72	2.36	0.60
$D(-4, 4)$	15.76	2.51	3.74	2.45	0.48
$D(-5, 5)$	19.14	2.51	3.75	2.51	0.44
$S(-3, 3)$	12.30	2.45	3.71	2.55	0.60
$S(-4, 4)$	15.76	2.47	3.65	2.93	0.40
$S(-5, 5)$	19.12	2.45	3.62	2.86	0.28
$S(-6, 6)$	22.41	2.46	3.60	2.84	0.24
$S(-7, 7)$	25.75	2.45	3.60	2.82	0.16
$S(-8, 8)$	29.14	2.46	3.60	2.82	0.12
$S(-9, 9)$	32.40	2.45	3.60	2.78	0.12
Monolayer	∞	2.45	3.57	2.76	0.00

[a] Wall thickness is defined by the radius difference between the inner and outer layers.

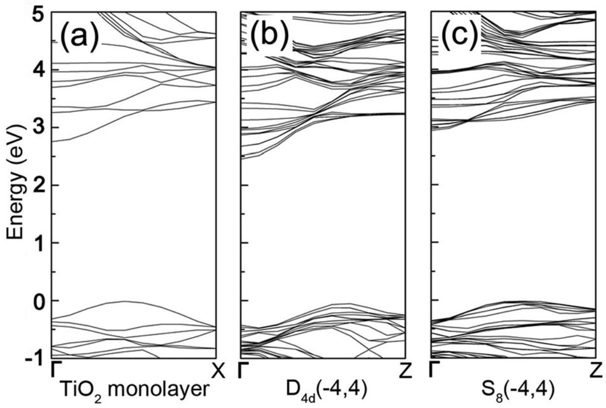

Fig. 2 Calculated band structures of (a) the TiO_2 monolayer, (b) (−4, 4) SWTONTs with D_{4d} and (c) S_8 symmetries. Here, the Fermi energy level is set to zero for clarity.

from 1.82 to 1.92, and from 1.82 to 1.87 Å for the $S_8(-4, 4)$ SWTONTs, respectively.

The calculated band structures of the TiO_2 monolayer, D_{4d} and $S_8(-4, 4)$ SWTONTs are plotted in Fig. 2(a)–(c), respectively. It is clear that the conduction band minimum (CBM) occurs at 2.76 eV, 2.45 eV, and 2.93 eV (all at Γ point), while the valence band maximum (VBM), set as the Fermi level, lies at the (0, 0, 0.225), (0, 0, 0.325) and (0, 0, 0.275) k-points for the TiO_2 monolayer, D_{4d} and $S_8(-4, 4)$ SWTONTs, respectively. This indicates that the TiO_2 monolayer and SWTONTs are all semiconductors with indirect band gaps. Note that the band gap of $D_{4d}(-4, 4)$ SWTONTs is 2.45 eV, which is smaller than that of the TiO_2 monolayer (2.76 eV) and $S_8(-4, 4)$ SWTONTs (2.93 eV). From the total density of states (DOS) and the projected DOS on Ti and O atoms in the TiO_2 monolayer, D_{4d} and $S_8(-4, 4)$ SWTONTs, as shown in Fig. 3, we were able to identify some characteristics of the band structures. The TDOS of these three systems have two well-separated broad peaks located at left and right sides of the Fermi level. The broad valence bands are mainly contributed by the O 2p orbitals, and the Ti 3d orbitals also made a considerable contribution, while the conduction bands are attributed to the Ti 3d orbitals. The narrowing and broadening of band gaps of D_{4d} and S_8 SWTONTs result from the downward and upward shifts in the conduction bands relative to the Fermi level, respectively. Actually, the PDOS feature of O atoms in the inner, middle and outer layers is distinguishable due to the different local surroundings, *i.e.* Ti–O bond lengths are slightly different in three layers.

The stability of SWTONTs is related to the ability of the structure to sustain the strain arising from different surface tensions existing at two sides of the rolled sheet. To evaluate the relative stability of these proposed SWTONTs, we calculated their strain energies (E_S), which is defined as $E_S = (E_{SWTONT} - E_{ML})/N$, where E_{SWTONT} and E_{ML} is the total energy of the SWTONTs and the TiO_2 monolayer with the same number of primary unit cells (N), respectively (each primary unit cell includes 4 Ti and 8 O atoms). Fig. 4(a) shows the calculated E_S of D_{nd} and S_{2n} SWTONTs with black squares and red triangles, respectively, and the strain energy of the TiO_2 monolayer is set to zero and plotted as a black dotted line. Obviously, these results for S_{2n} SWTONTs agree well with the previous reports.[23,25] Given the almost same diameter, the E_S of S_{2n} SWTONTs is slightly smaller than that of SWTONTs with D_{nd} symmetry. And the strain energy difference between SWTONTs with two different symmetries increases with an increase of their diameters. For example, the E_S values of the $D_{nd}(-4, 4)$ and $(-5, 5)$ SWTONTs are predicted to be 0.48 and 0.44 eV, which are larger than those of SWTONTs with S_{2n} symmetry (0.40 and 0.28 eV). These results imply that the SWTONTs energetically prefer the S_{2n} structures. These positive strain energies indicate that these SWTONTs are less stable than the corresponding TiO_2 monolayers, although for these SWTONTs with large diameters, E_S gradually decreases, and at last it approaches zero (E_S of the TiO_2 monolayer). It should be pointed out that these observations are different from those of a previous theoretical study on TiO_2 nanotubes rolled up from an anatase (001) sheet with a thickness of three monolayers.[26] Ferrari *et al.* have predicted that strain energies will be negative for TiO_2 nanotubes with diameters ranging from 3.3 to 6.6 nm, which provides a possible explanation for the rolling-up of the TiO_2 nanotubes in experiments.[26]

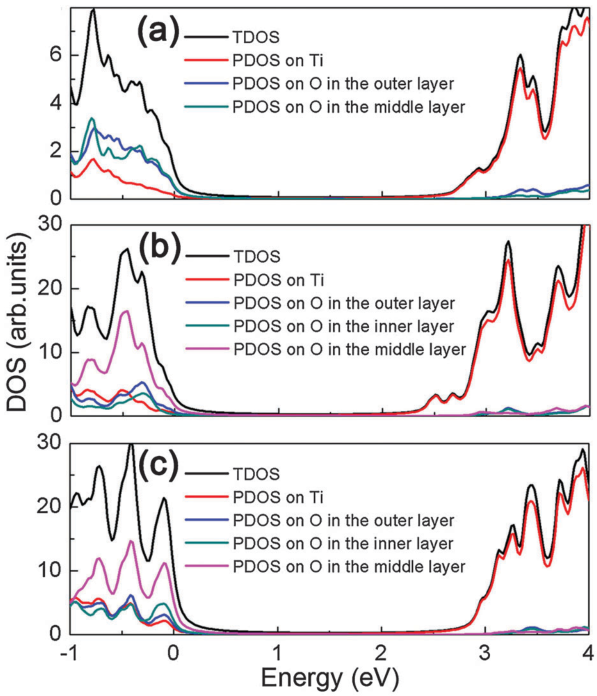

Fig. 3 Calculated total DOS and partial DOS projected on different atomic layers in (a) the TiO_2 monolayer, (b) $D_{4d}(-4, 4)$, and (c) $S_8(-4, 4)$ TiO_2 nanotubes. The Fermi energy level is set to zero.

To qualitatively explain the above strain energy results, we analyzed the optimized lattice constants (c) along the tube axis (Z direction) and the Ti–O distances in SWTONTs. Fig. 4(b) shows the optimized c of D_{nd} and S_{2n} SWTONTs. Clearly, the change tendency of the c values is different for the SWTONTs with two symmetries. With an increase of the diameter (D), the

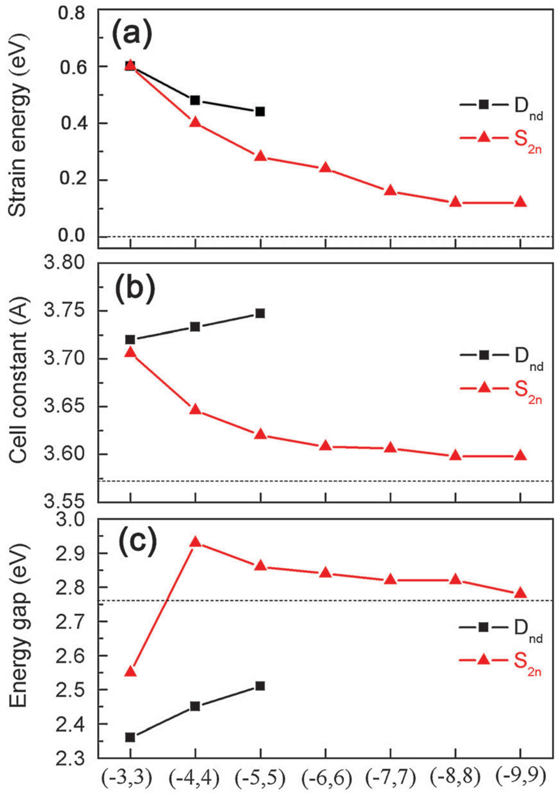

Fig. 4 (a) Strain energies (E_S) of D_{nd} and S_{2n} SWTONTs with different sizes (n). (b) Lattice constant (c) of SWTONTs, (c) band gaps (E_g) of SWTONTs. Here, the corresponding values of the TiO_2 monolayer are plotted as black dotted lines.

c of D_{nd} SWTONTs increases, while it gradually decreases for S_{2n} SWTONTs. For $n = 3$–5, the c values and the wall thicknesses (T) of D_{nd} SWTONTs are larger than those of SWTONTs with S_{2n} symmetry, while their diameters are very similar. For example, the values of c, T and D of $D_{4d}(-4, 4)$ SWTONTs are 3.74, 2.51 and 15.76 Å, respectively, with the corresponding values of 3.65, 2.47 and 15.76 Å for $S_8(-4, 4)$ SWTONTs. Compared with the TiO_2 monolayer, the Ti–O distances are somewhat elongated in SWTONTs with two different symmetries, which originate from the elongated c in SWTONTs. The wall thickness difference combined with the optimized c values shown in Fig. 4(b) can be used to qualitatively understand the calculated E_S results. Compared with the D_{nd} structure, these S_{2n} SWTONTs have relatively small wall thicknesses, which result in the relatively small strain energies, as shown in Fig. 4(a).

Fig. 4(c) shows the predicted band gaps (E_g) of SWTONTs. It is clear that the band gaps of all SWTONTs are significantly larger than that of TiO_2 bulk. The band gaps of S_{2n} SWTONTs ($n \geq 4$) and D_{nd} SWTONTs ($n = 3$–5) are larger and less than that of the TiO_2 monolayer (2.76 eV), and they decrease and increase when their diameters increase, respectively. For example, the band gaps of the $(-4, 4)$ and $(-5, 5)$ SWTONTs with D_{nd} (S_{2n}) symmetry are 2.45 (2.93) and 2.51 (2.86) eV. The calculated E_S and c values of the D_{3d} SWTONTs are predicted to be 0.60 eV and 3.72 Å, which are close to the corresponding values (0.60 eV and 3.71 Å) of the S_6 SWTONT ($n = 3$, the smallest diameter), while they have considerable different band gaps of 2.36 and 2.55 eV, respectively. Note that the $S_8(-4, 4)$ SWTONTs have the largest band gap of 2.93 eV. Clearly, when n changes from 3 to 4, the band gap of SWTONT abruptly increases, similar to the previous reports,[22,23,25] which may be ascribed to the symmetry and the slightly shortened lattice constant (c).

It is well known that the elastic properties are strongly related to the geometric and electronic properties.[58] Finally, we examined the elastic properties of the SWTONTs with two different symmetries. For these SWTONTs, the Young's modulus (Y) can be calculated by $Y = (\partial^2 E/\partial \varepsilon^2)/V_0$, where E is the strain energy per unit cell, and ε is the axial strain, defined as c/c_0 where c_0 is the lattice constant of the unit cell at mechanical equilibrium, V_0 is the equilibrium volume $V_0 = 2\pi R \times c_0 \times T$, where R is the radius and T is the tube wall thickness, which is defined by the radius difference between the inner and outer layers. The calculated Young's moduli of $D_{3d}(-3, 3)$ and $D_{4d}(-4, 4)$ SWTONTs are 145.9 and 168.2 GPa, which are larger than that of $S_6(-3, 3)$ and $S_8(-4, 4)$ nanotubes (100.7 and 92.5 GPa). These values are significantly less than that of TiO_2 nanotubes rolled up along the rutile (001) surface.[29] Clearly, compared with the $S_{2n}(-n, n)$ nanotubes, the $D_{nd}(-n, n)$ SWTONTs are more stiff due to their relatively large strain energies, as shown in Fig. 4(a). These results indicate that the electronic and mechanical properties of anatase SWTONTs can be effectively tuned by the symmetry, dimensions and atomic arrangement.

B. TiO_2 nanotube arrays

Compared with extensive experimental studies on the preparations and applications of TONTAs, the corresponding theoretical attention is very limited so far. Our previous investigation focused on the rutile $TiO_2(110)$ and anatase (001) nanotube arrays.[28,45] Here, we turn to examine the anatase TONTAs with different apertures, constructed from $TiO_2(101)$ bilayers, as shown in Fig. 5(a). In some experiments, the TONTAs have hexagonal compact packing.[11–13] Here, we focused on the TONTAs having hexagonal compact packing with two different sizes, labeled as A6 and A12 in Fig. 5(b) and (c), respectively. The core and bridge regions, which are shared with three and two neighboring nanotubes, in the proposed hexagonal TONTAs are illustrated with red ring and blue box in Fig. 5(b) and (c), respectively, for clarity. The insets in the right panel of Fig. 5(b) and (c) are the amplified pictures of the core and bridge regions. The centre hole of the core region can be seen as a nanotube rolled up along the (001) surface, which is in accord with the fact that the TONTAs prefer the (004) orientation along the anatase TiO_2 tube axis.[11] The optimized results show that the Ti–O distances at the core and bridge regions vary from 1.78 to 2.11 Å, and from 1.85 to 2.12 Å, respectively. These Ti–O bond lengths change slightly compared to that of the TiO_2 bilayer (varying from 1.82 to 2.13 Å).

Similar to SWTONTs, we compared two TONTAs with different apertures. We firstly calculated the strain energies (E_S) of the TONTAs. Here, the E_S is also defined as $E_S = (E_{TONTA} - E_{BL})/N$, where E_{TONTA} and E_{BL} are the total energies of TONTAs and the

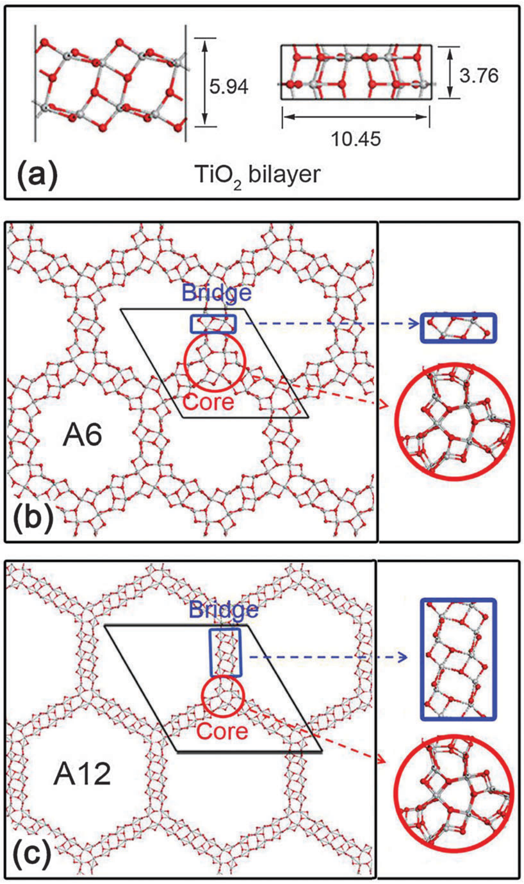

Fig. 5 (a) The side and top views of a TiO_2 bilayer, (b) the top view along the tube axis of the A6 TONTA, (c) the A12 TONTA. Here, the red ring and the blue box stand for the core and bridge regions in TONTAs, respectively.

TiO_2 bilayer with the same number of primary unit cells (N), respectively. The calculated E_S values of A6 and A12 TONTAs are 0.40 and 0.20 eV, respectively. These results imply that the TONTAs will be more stable with increasing apertures. At the same time, the lattice constant (c) is almost fixed (3.77 Å) which is close to the value 3.76 Å of the bilayer. The E_g of all TONTAs is about 2.36 eV, which is not sensitive to their apertures. This value is larger than that of TiO_2 bulk (1.92 eV), but it is less than that of the TiO_2 bilayer (2.66 eV).

To understand the narrowing of band gaps in TONTAs, we calculated band structures and the total DOS of the A12 TONTA as examples. The ground states of TONTAs are all spin-restricted. Clearly, the calculated band structures of the A12 TONTA, as shown in Fig. 6(a), show that it is a semiconductor with an indirect band gap of about 2.36 eV, which is less than that of the TiO_2 bilayer (2.66 eV). The total DOS of the A12 TONTA and the TiO_2 bilayer are plotted in Fig. 6(b). There are edge states appearing within the band gap of the TiO_2 bilayer, which narrow the band gap of the A12 TONTA. To describe these edge states, the spatial distributions of the VBM at the (0, 0, 0.325) k-point and the CBM at the Γ point are plotted in the right panel of Fig. 6(a). Obviously, both CBM and VBM are all localized around the core region.

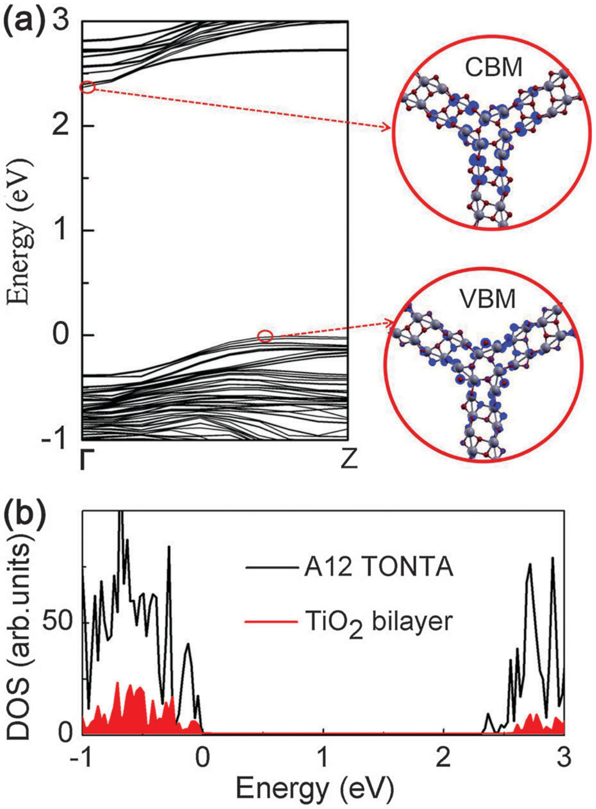

Fig. 6 (a) The band structures of the A12 TONTA, and the spatial distributions of the CBM and the VBM, (b) the total DOS of the A12 TONTA, here, the red shadow is the total DOS of the TiO_2 bilayer.

To demonstrate the energy gap modification in more detail, we calculated the partial DOS of Ti and O atoms in the core and bridge regions of the A12 TONTA, as shown in Fig. 7. It is clear that these observed edge states at both CBM and VBM mainly arise from the Ti and O atoms in the core. The shape of the partial DOS of the bridge region is similar to that of the TiO_2 bilayer. After further analysis, we found that the CBM is mainly contributed by the Ti $3d_{xz}$ and $3d_{yz}$ atomic orbitals, while the O 2p orbitals made the dominant contribution to the VBM.

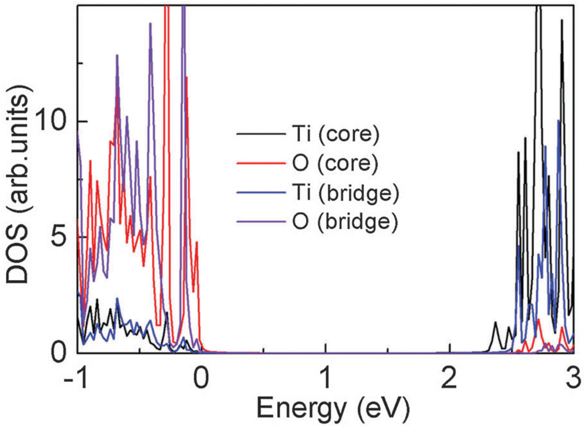

Fig. 7 Partial DOS of O and Ti atoms in the core and bridge regions of the A12 TONTA.

C. Optical properties of SWTONTs and TONTAs

In experiments, a key performance indicator of TiO_2 nanostructures is the optical absorption, which always significantly depends on their morphology, dimensions and size.[20,21] Especially, the anatase TiO_2 tubes could display a strongly enhanced photocurrent compared with a compact TiO_2 film.[59] Now we turn to calculate the optical absorptions of these examined SWTONTs and TONTAs by using the following equation,[60]

$$\alpha_{\text{abs}} = \sqrt{2}\omega\left(\sqrt{\varepsilon_1{}^2(\omega) + \varepsilon_2{}^2(\omega)} - \varepsilon_1(\varepsilon)\right)^{\frac{1}{2}}$$

where $\varepsilon_1(\omega)$ and $\varepsilon_2(\omega)$ are the real and imaginary parts of the frequency dependent complex dielectric function $\varepsilon(\omega)$, respectively. Taking into account the tensor nature of the dielectric function, $\varepsilon_1(\omega)$ and $\varepsilon_2(\omega)$ are averaged over three polarization vectors (along x, y, and z directions). The frequency and dimension dependent optical coefficients of SWTONTs and TONTAs are obtained by calculating the optical transition matrix elements between the valence and conduction subbands. In our calculations, the real and imaginary parts of the dielectric function ε_1 and ε_2 along vertical and parallel directions relative to the tube axis were evaluated.

For example, Fig. 8(a) and (b) show the optical properties of the $S_8(-4, 4)$ SWTONT and A12 TONTA, and the results for the TiO_2 monolayer and a bilayer are also shown for comparison, respectively. Following two features were observed. The first one is that compared with the TiO_2 monolayer and bilayer, the blue and red absorption onsets are observed for the $S_8(-4, 4)$ SWTONT and A12 TONTA, respectively. This observation is consistent with their corresponding relative values of E_g. Namely, the E_g values of the $S_8(-4, 4)$ SWTONT and A12 TONTA are 2.93 and 2.36 eV, which are larger and less than that of the TiO_2 monolayer (2.76 eV) and bilayer (2.66 eV), respectively. These results indicate that the optical absorption properties of TONTAs are better than that of SWTONTs due to the narrowed band gap. The second feature is that we observe a noticeable difference in absorption spectra that occurs depending on the polarization direction (whether in radial or axial) of the electric field of the incoming light. Similar to the previous investigation on anatase TiO_2 nanotubes rolled up from a (101) layer along the [−101] direction,[24] a significant optical anisotropy appears for all examined SWTONTs and TONTAs. As for the TiO_2 monolayer, the optical absorption coefficients along the vertical direction with the photon energy (range, 2.5–3.5 eV) are significantly larger than that in the parallel direction. Similar features are observed for the TiO_2 bilayer. In contrast, as for the $S_8(-4, 4)$ SWTONT and A12 TONTA, the optical absorption coefficients along the parallel direction have larger values compared with the corresponding results along the vertical direction.

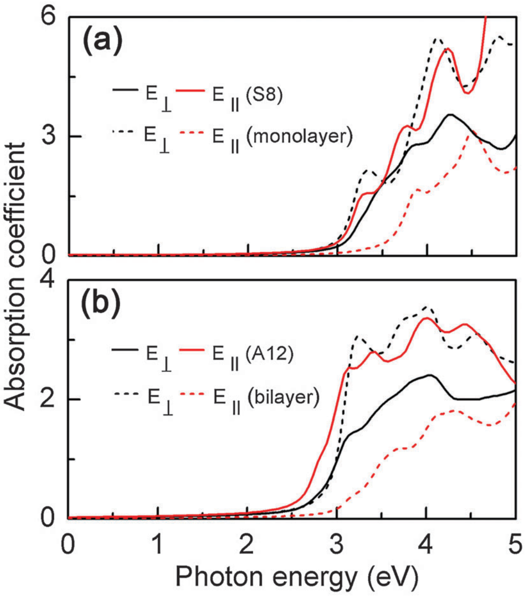

Fig. 8 Optical absorption coefficients are plotted in black and red full lines for two different directions within the photon energy range of 0–5 eV. (a) The (−4, 4) SWTONT with S_8 symmetry. (b) The A12 TONTA. Here, ⊥ and ∥ stand for the vertical and parallel directions relative to the tube axis (Z direction), respectively, and the corresponding optical absorption coefficients of the relative monolayers and bilayers are also plotted as dotted lines for comparison.

Clearly, the optical properties of TiO_2 nanostructures are strongly related to their atomic arrangement and the direction of injecting light. The absorption coefficients can be enhanced by packing TiO_2 sheets into compact hexagonal arrays. On the other hand, it should be pointed out that the carrier transport along one-dimensional nanostructures could be more efficient than within a three-dimensional random network of nanoparticles, where the electrons have to cross many particle boundaries. The examined SWTONTs and TONTAs should improve the collection of the photogenerated carriers since they have electron percolation pathways for vectorial charge transfer between interfaces.[3,41,59] In closing, we hope that these presented theoretical findings will stimulate further experimental studies on the SWTONTs and TONTAs.

Conclusions

In summary, we performed comprehensive DFT calculations to explore the stability, electronic structures and optical absorption properties of the SWTONTs and TONTAs constructed from anatase TiO_2(101) sheets. As for SWTONTs, we find that the lattice constants (c), strain energies (E_S) and band gaps (E_g) of D_{nd} and S_{2n} SWTONTs can be effectively tuned by changing their diameters. We obtained the stable D_{nd} (n = 3–5) SWTONTs. All SWTONTs energetically prefer the S_{2n} structure. Upon increasing their radius, the corresponding calculated c, E_S and E_g values showed different change tendencies for two different symmetries. The calculated Young's moduli of $D_{nd}(-n, n)$ nanotubes are much stiffer than that of $S_{2n}(-n, n)$ nanotubes along the tube axis (Z direction) due to the relatively large strain energies. The band gaps of TONTAs are all close to 2.36 eV, which are less than that of TiO_2 bilayers. The narrow band gaps of TONTAs originate from the edge states mainly contributed by the Ti and O atoms at the core region. The tunable optical absorptions of these examined SWTONTs and TONTAs display anisotropic behaviour. These theoretical findings verify that the electronic and optical properties of TiO_2 nanostructures are determined by their symmetry, dimensions and morphology, which provide useful information to understand the related experimental observations.

Acknowledgements

This work was partially supported by the National Key Basic Research Program (Nos. 2011CB921400 and 2014CB921101), the Strategic Priority Research Program (B) of the CAS (No. XDB01020000), the National Natural Science Foundation of China (Nos. 21273208, 11034006, and 21121003), the Anhui Provincial Natural Science Foundation (1408085QB26), the Fundamental Research Funds for the Central Universities, the China Postdoctoral Science Foundation (No. 2012M511409), CAS, USTC and Shanghai Supercomputer Centers.

Notes and references

1 V. Zwilling, E. Darque-Ceretti, A. Boutry-Forveille, D. David, M. Y. Perrin and M. Aucouturier, *Surf. Interface Anal.*, 1999, **27**, 629–637.

2 V. Zwilling, M. Aucouturier and E. Darque-Ceretti, *Electrochim. Acta*, 1999, **45**, 921–929.

3 P. Roy, S. Berger and P. Schmuki, *Angew. Chem., Int. Ed.*, 2011, **50**, 2904–2939.

4 D. V. Bavykin, J. M. Friedrich and F. C. Walsh, *Adv. Mater.*, 2006, **18**, 2807–2824.

5 J. C. Hulteen and C. R. Martin, *J. Mater. Chem.*, 1997, **7**, 1075–1087.

6 T. Kasuga, M. Hiramatsu, A. Hoson, T. Sekino and K. Niihara, *Adv. Mater.*, 1999, **11**, 1307–1311.

7 D. Gong, C. A. Grimes, O. K. Varghese, W. C. Hu, R. S. Singh, Z. Chen and E. C. Dickey, *J. Mater. Res.*, 2001, **16**, 3331–3334.

8 M. S. Sander, M. J. Côté, W. Gu, B. M. Kile and C. P. Tripp, *Adv. Mater.*, 2004, **16**, 2052–2057.

9 S. P. Albu, D. Kim and P. Schmuki, *Angew. Chem., Int. Ed.*, 2008, **120**, 1942–1945.

10 B. Mandlmeier, J. M. Szeifert, D. Fattakhova-Rohlfing, H. Amenitsch and T. Bein, *J. Am. Chem. Soc.*, 2011, **133**, 17274–17282.

11 Y. Yang, X. H. Wang and L. T. Li, *J. Am. Ceram. Soc.*, 2008, **91**, 632–635.

12 S. Q. Li, G. M. Zhang, D. Z. Guo, L. G. Yu and W. Zhang, *J. Phys. Chem. C*, 2009, **113**, 12759–12765.

13 L. Zhang and Y. Han, *Nanotechnology*, 2010, **21**, 055602.

14 G. K. Mor, K. Shankar, M. Paulose, O. K. Varghese and C. A. Grimes, *Nano Lett.*, 2006, **6**, 215.

15 Q. Zheng, B. X. Zhou, J. Bai, L. H. Li, Z. J. Jin, J. L. Zhang, J. H. Li, Y. B. Liu, W. M. Cai and X. Y. Zhu, *Adv. Mater.*, 2008, **20**, 1044–1049.

16 D. A. Wang, Y. Liu, C. W. Wang, F. Zhou and W. M. Liu, *ACS Nano*, 2009, **3**, 1249–1257.

17 K. Shankar, J. Bandara, M. Paulose, H. Wietasch, O. K. Varghese, G. K. Mor, T. J. LaTempa, M. Thelakkat and C. A. Grimes, *Nano Lett.*, 2008, **8**, 1654–1659.

18 N. K. Allam, K. Shankar and C. A. Grimes, *J. Mater. Chem.*, 2008, **18**, 2341–2348.

19 O. K. Varghese, M. Paulose, T. J. LaTempa and C. A. Grimes, *Nano Lett.*, 2009, **9**, 731–737.

20 B. S. Liu, K. Nakata, S. H. Liu, M. Sakai, T. Ochiai, T. Murakami, K. Takagi and A. Fujishima, *J. Phys. Chem. C*, 2012, **116**, 7471–7479.

21 S. Z. Liang, J. F. He, Z. H. Sun, Q. H. Liu, Y. Jiang, H. Cheng, B. He, Z. Xie and S. Q. Wei, *J. Phys. Chem. C*, 2012, **116**, 9049–9053.

22 A. V. Bandura and R. A. Evarestov, *Surf. Sci.*, 2009, **603**, L117–L120.

23 R. A. Evarestov, A. V. Bandura, M. V. Losev, S. Piskunov and Y. F. Zhukovskii, *Physica E*, 2010, **43**, 266–278.

24 F. M. Hossain, A. V. Evteev, I. V. Belova, J. Nowotny and G. E. Murch, *Comput. Mater. Sci.*, 2010, **48**, 854–858.

25 R. A. Evarestov, Y. F. Zhukovskii, A. V. Bandura and S. Piskunov, *Cent. Eur. J. Phys.*, 2011, **9**, 492–501.

26 A. M. Ferrari, D. Szieberth, C. M. Zicovich-Wilson and R. Demichelis, *J. Phys. Chem. Lett.*, 2010, **1**, 2854–2857.

27 Q. Q. Meng, J. G. Wang, Q. Xie and X. N. Li, *J. Phys. Chem. C*, 2010, **114**, 9251–9256.

28 Q. Q. Meng, J. G. Wang, Q. Xie, H. Q. Dong and X. N. Li, *Catal. Today*, 2011, **165**, 145–149.

29 T. He, M. W. Zhao, X. J. Zhang, H. Y. Zhang, Z. H. Wang, Z. X. Xi, X. D. Liu, S. S. Yan, Y. Y. Xia and L. M. Mei, *J. Phys. Chem. C*, 2009, **113**, 13610–13615.

30 J. N. Hart, S. C. Parker and A. A. Lapkin, *ACS Nano*, 2009, **3**, 3401–3412.

31 H. Y. Zhang and S. L. Dong, *Chin. Phys. Lett.*, 2013, **30**, 043102.

32 W. F. Huang, P. J. Wu, W. C. Hsu, C. W. Wu, K. S. Liang and M. C. Lin, *J. Theor. Comput. Chem.*, 2013, **12**, 1350007.

33 R. A. Evarestov, Y. F. Zhukovskii, A. V. Bandura and S. Piskunov, *J. Phys. Chem. C*, 2010, **114**, 21061–21069.

34 A. M. Ferrari, D. Szieberth and Y. Noel, *J. Mater. Chem.*, 2011, **21**, 4568–4580.

35 R. A. Evarestov, Y. F. Zhukovskii, A. V. Bandura, S. Piskunov and M. V. Losev, *J. Phys. Chem. C*, 2011, **115**, 14067–14076.

36 A. M. Ferrari, M. Lessio, D. Szieberth and L. Maschio, *J. Phys. Chem. C*, 2010, **114**, 21219–21225.

37 D. Szieberth, A. M. Ferrari, P. D'Arco and R. Orlando, *Nanoscale*, 2011, **3**, 1113–1119.

38 D. Szieberth, A. M. Ferrari, Y. Noel and M. Ferrabone, *Nanoscale*, 2010, **2**, 81–89.

39 D. J. Mowbray, J. I. Martinez, J. M. García Lastra, K. S. Thygesen and K. W. Jacobsen, *J. Phys. Chem. C*, 2009, **113**, 12301–12308.

40 J. G. Wang, L. Wang, L. Ma, J. J. Zhao, B. L. Wang and G. H. Wang, *Physica E*, 2009, **41**, 838–842.

41 F. M. Hossain, A. V. Evteev, I. V. Belova, J. Nowotny and G. E. Murch, *Adv. Appl. Ceram.*, 2012, **111**, 72–93.

42 F. Lin, G. Zhou, Z. Y. Li, J. Li, J. Wu and W. H. Duan, *Chem. Phys. Lett.*, 2009, **475**, 82–85.

43 C. K. Dong, X. Li and J. Y. Qi, *J. Phys. Chem. C*, 2011, **115**, 20307–20315.

44 F. Nunzi and F. De Angelis, *J. Phys. Chem. C*, 2011, **115**, 2179–2186.

45 X. Pan, Q. X. Cai, W. L. Chen, G. L. Zhuang, X. N. Li and J. G. Wang, *Comput. Mater. Sci.*, 2013, **67**, 174–181.

46 G. Kresse and J. Hafner, *Phys. Rev. B: Condens. Matter Mater. Phys.*, 1993, **47**, 558–561.

47 P. E. Blöchl, *Phys. Rev. B: Condens. Matter Mater. Phys.*, 1994, **50**, 17953–17979.

48 J. P. Perdew, K. Burke and M. Ernzerhof, *Phys. Rev. Lett.*, 1996, **77**, 3865–3868.

49 J. Heyd, G. E. Scuseria and M. Ernzerhof, *J. Chem. Phys.*, 2003, **118**, 8207–8215.

50 J. Heyd and G. E. Scuseria, *J. Chem. Phys.*, 2004, **120**, 7274–7280.

51 V. I. Anisimov, J. Zaanen and O. K. Andersen, *Phys. Rev. B: Condens. Matter Mater. Phys.*, 1991, **44**, 943–954.

52 V. I. Anisimov, F. Aryasetiawan and A. I. Lichtenstein, *J. Phys.: Condens. Matter*, 1997, **9**, 767–808.

53 G. S. Shao, *J. Phys. Chem. C*, 2009, **113**, 6800–6808.

54 J. K. Burdett, T. Hughbanks, G. J. Miller, J. W. Richardson, Jr. and J. V. Smith, *J. Am. Chem. Soc.*, 1987, **109**, 3639–3646.

55 T. Ziegler, *A chronicle about the development of electronic structure theories for transition metal complexes*, Springer-Verlag, Berlin, Heidelberg, 2011, pp. 1–38.

56 J. L. F. Da Silva, M. V. Ganduglia-Pirovano, J. Sauer, V. Bayer and G. Kresse, *Phys. Rev. B: Condens. Matter Mater. Phys.*, 2007, **75**, 045121.

57 N. J. Mosey and E. A. Carter, *Phys. Rev. B: Condens. Matter Mater. Phys.*, 2007, **76**, 155123.

58 X. J. Wu, Z. P. Xu and X. C. Zeng, *Nano Lett.*, 2007, **7**, 2987–2992.

59 R. Beranek, H. Tsuchiya, T. Sugishima, J. M. Macak, L. Taveira, S. Fujimoto, H. Kisch and P. Schmuki, *Appl. Phys. Lett.*, 2005, **87**, 243114.

60 M. Gajdoš, K. Hummer, G. Kresse, J. Furthmller and F. Bechstedt, *Phys. Rev. B: Condens. Matter Mater. Phys.*, 2006, **73**, 045112.